Journal of Magnetism and Magnetic Materials 482 (2019) 376–381

Contents lists available at ScienceDirect

Journal of Magnetism and Magnetic Materials

journal homepage: www.elsevier.com/locate/jmmm

Compositional variation of amorphous phase controlled coercivity of $Nd_{60}Fe_{30}Al_{10}$ alloy

ARTICLE INFO

Keywords:
Amorphous alloys
Microstructure
Coercivity mechanism

ABSTRACT

The coercivity of Nd-Fe-Al amorphous ferromagnetic materials originates from the combination of magnetic interaction and strong pinning of domain walls. Using $Nd_{60}Fe_{30}Al_{10}$ alloys made under three cooling rates, we discovered an important microstructure parameter that can be used to strengthen interaction and pinning. By tuning the variations of composition difference between Nd-rich and Fe-rich amorphous regions, we enhanced the magnetic interaction and increased maximum restoring force per pin of Nd nanocrystals (with size < 30 nm embedded in amorphous matrix). We were, however, not able to change pinning force by changing the grain morphology and the size of Nd nanocrystals (< 30 nm).

1. Introduction

Since the first report on $Nd_{60}Fe_{30}Al_{10}$ bulk amorphous alloys (BAAs) in 1996, there has been growing interest in these alloys because of their hard magnetic properties at room temperature, and as a consequence they may be possible candidates for use as permanent magnets [1,2]. The hard magnetic behavior of the Nd-based amorphous alloys is surprising, given that disorder of the amorphous state usually produces magnetic softness rather than hardness. Furthermore, it is of interest to note that the current coercivity mechanisms [3], e.g. the shape anisotropy, magnetocrystalline anisotropy, and nucleation of domain model, used widely in permanent alloys, cannot explain adequately the hard magnetic behavior of Nd-based BAAs at room temperature. Therefore, understanding the coercivity mechanism of Nd-based BAAs has a significant impact on developing this type of permanent magnets.

Although the term *amorphous* is used, the common feature of the microstructure in Nd-based alloys is the presence of clusters or nanocrystals, which vary in diameter from 1.2 nm to 50 nm, embedded in an amorphous matrix in these materials [4–8]. On the basis of such a microstructure, a number of mechanisms have been proposed to explain coercivity in Nd-based amorphous alloys. For example, Inoue et al. [1] proposed a random anisotropy model and suggested that the coercivity in Nd-Fe-Al BAAs originated from the homogeneous dispersion of Nd-Fe and Nd-Fe-Al clusters with large random magnetic anisotropy. McCallum and his co-workers suggested that the coupling of the δ – phase ($Nd_6Fe_{13-x}Al_{1+x}$, $1 < x < 4.5$) with a size of 1.2 nm to the ferromagnetic matrix in an "exchange-bias"-type manner conferred high values of coercivity in melt-spun Nd-Fe-Al alloys [6]. Other researchers used strong pinning model of domain walls to describe the coercivity mechanism in Nd-based BAAs [9–15]. In our previous work, the coercivity (286 kA/m) in $Nd_{60}Fe_{30}Al_{10}$ BAA was proposed to be from the combination of magnetic interaction and strong pinning of domain walls [16]. The remaining important question is which microstructure parameter affects interaction and domain wall pinning. In our present study, we prepared samples with different cooling rate to elaborate how the nanocrystals in the amorphous phase and the chemistry compositions of the amorphous phase affect the coercivity. We observed α-Nd nanocrystals with a size of 5–40 nm in both melt-spun ribbons and rod samples of 2 mm in diameter. The grain morphology and the average grain size (< 30 nm) of Nd nanocrystals appear to have minor effects on the maximum restoring force per pin. The composition gap between Nd-rich and Fe-rich amorphous phases of $Nd_{60}Fe_{30}Al_{10}$ alloy influences both the magnetic interaction and the pinning of domain walls.

2. Material and methods

Ingots with nominal composition $Nd_{60}Fe_{30}Al_{10}$ were prepared by arc-melting in an argon atmosphere from 99.99% pure Nd, Fe, and Al from Trillion Metals Co., Beijing. Ingots were re-melted four times for homogenization. Ribbon samples were prepared by melt-spinning in an argon atmosphere on a water-cooled copper wheel at speed of 5 m/s (labeled as M5), 10 m/s (labeled as M10), 15 m/s, 20 m/s, 25 m/s and 35 m/s. Rods of 2 mm in diameter and 40 mm in length were obtained by suction-casting the molten alloy into a water-cooled copper mold and numbered as C2, see Table 1. Magnetic properties were measured at room temperature on a Lake Shore 7407 vibrating sample magnetometer (VSM) with a maximum field of 1.8 T. The magnetic properties decreased with increasing the wheel speed of ribbons samples, as shown in Supplementary Fig. S1. The Henkel plot was determined from the isothermal remanence magnetization (IRM) and DC demagnetization (DCD) curves [17]. Henkel plots of $Nd_{60}Fe_{30}Al_{10}$ ribbon samples were constructed for ribbon samples at various wheel speed (Supplementary Fig. S2). We chose ribbon samples M5, M10 and a rod sample C2 for further investigations. The width of the domain wall was determined by measuring the intrinsic coercivity as a function of sweeping rate of applied field as described in Supplementary Fig. S3. Structure was characterized on a D/max-2550 X-ray diffractometer (XRD) with Cu Kα radiation, a GAIA3 scanning electron microscope (SEM) and a JEM 2100F transmission electron microscope (TEM) operating at 200 kV. The TEM samples and atom probe tomography (APT) needle specimens were prepared using an FEI HELIOS NanoLab 600i focused ion beam (FIB). The APT characterizations were carried out in a CAMECA Instruments LEAP4000X HR local electrode atom probe. The specimens were analyzed in laser mode with a specimen temperature at 50 K with

https://doi.org/10.1016/j.jmmm.2019.03.059
Received 2 January 2019; Received in revised form 11 February 2019; Accepted 9 March 2019
Available online 11 March 2019
0304-8853/

Table 1
The saturation magnetization, M_s, the remanent magnetization, M_r, the intrinsic coercivity, H_c^i, the domain wall width, δ_w, the maximum restoring force per pin, f, the average grain size, d, and the morphology of Nd nanocrystals for melt-spun $Nd_{60}Fe_{30}Al_{10}$ samples prepared at the wheel speed of 10 m/s and 5 m/s, and as-cast $Nd_{60}Fe_{30}Al_{10}$ rod sample of 2 mm in diameter.

Samples	Condition	M_s (Am^2/kg)	M_r (Am^2/kg)	H_c^i (kA/m)	δ_w (nm)	$f \times 10^{-11}$ (N)	d(nm)	morphology of Nd nanocrystals
M10	melt-spun, 10 m/s	19.6	10.1	169	28	1.4	10 ± 3	granular
M5	melt-spun, 5 m/s	21.8	13.3	214	27	1.5	24 ± 8	flake
C2	as-cast,ϕ 2 mm	22.1	14.6	287	13	3.4	25 ± 7	flake

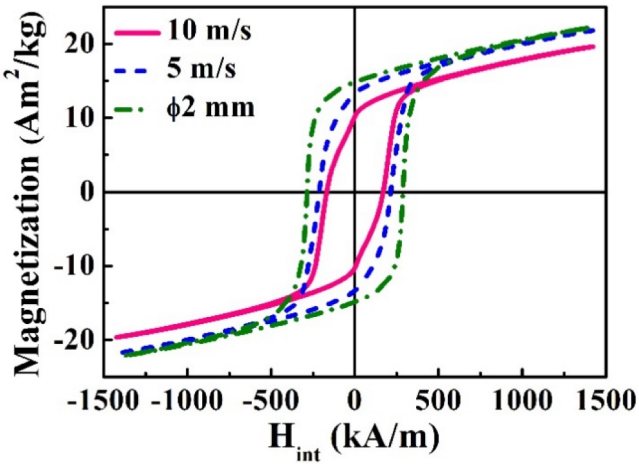

Fig. 1. Hysteresis loops of samples M10, M5 and C2.

a target evaporation rate of 1%, the energy of pulse laser is 60 pJ, and a vacuum < 10^{-8} Pa.

3. Results

The hysteresis loops (Fig. 1) at room temperature show single phase hard magnetic behavior in samples M10, M5 and C2. The key magnetic parameters are shown in Table 1. The saturation magnetization (M_s) values are almost the same for three conditions. The remanent magnetization, M_r, increases monotonically by an order of M10 < M5 < C2. The intrinsic coercivity (H_c^i) increases by 70% from 169 kA/m of sample M10 to 287 kA/m of sample C2.

Based on Wohlfarth model, Henkel plot is an effective method to understand the phenomenon of magnetic interaction [18,19]. Henkel plots of all samples with positive deviations (marked by an arrow) indicate that magnetic interaction occurs in all samples and the interaction increases monotonically from sample M10 to sample C2 (Fig. 2a). We used the vertical distance from the highest point in the positive deviation to the non-interaction line (marked as a dash line) to quantify the strength of interaction. The ratio of the vertical distance is 3: 1.9: 1 for samples M10, M5 and C2.

For the case of strong pinning of domain walls developed by Gaunt [9], the value of H_c^i, as a function of temperature, T, is given by

$$\left(\frac{H_c^i}{H_0}\right)^{1/2} = 1 - \left(\frac{75k_BT}{4bf}\right)^{2/3} \quad (1)$$

where H_0 is the critical field at $T = 0$ K, k_B is Boltzmann constant, $4b$ is the interaction range of a pin equating with the domain wall width, δ_w, and f is the maximum restoring force per pin.

Eq. (1) can be rewritten as

$$(H_c^i)^{1/2} = b^* + c(T)^{2/3} \quad (2)$$

where $b^* = (H_0)^{1/2}$ and $c = (H_0)^{1/2}(75k_B/(4bf))^{2/3}$.

The simple linear relationship between $(H_c^i)^{1/2}$ and $T^{2/3}$ demonstrates a very good agreement with the strong pinning domain wall model in all samples (Fig. 2b). Hence, the Henkel plot result and good agreement with relation (2) indicate that the coercivity in melt-spun $Nd_{60}Fe_{30}Al_{10}$ ribbons and as-cast rod sample is from a combination of both interaction and strong pinning of domain walls. The data shown in Fig. 2b was fitted with a standard linear least-squares method to Eq. (2), and the constants b^* and c were determined. The value of $4b$, or δ_w, was calculated by H_c^i as a function of sweeping rate, see Supplementary Fig. S3. The calculated value of the maximum restoring force per pin (f) from $c = (H_0)^{1/2}(75k_B/(4bf))^{2/3}$ indicated that f (3.4×10^{-11} N) for sample C2 was greater than 2 times of that in samples M10 ($f = 1.4 \times 10^{-11}$ N) and M5 ($f = 1.5 \times 10^{-11}$ N). The data in Fig. 2 suggests that to enhance the coercivity for $Nd_{60}Fe_{30}Al_{10}$ amorphous alloys, both magnetic interaction and pinning force for domain walls have to be improved. To further investigate the relative importance of these two factors, the microstructure was studied.

XRD patterns of all samples are similar with some diffraction peaks identified as α-Nd superimposing on the broad amorphous peaks (Supplementary Fig. S4). Back-scattered SEM image shows featureless contrast in sample M10 (see Supplementary Fig. S5a), indicating a homogeneous microstructure. Sample M5 exhibits regions with different contrast in nano-scale (see Supplementary Fig. S5b). TEM images show that nanocrystals of 5–18 nm and 10–40 nm in size, embedded in the amorphous phase in samples M10 and M5, respectively (Fig. 3a and 3b). High-resolution TEM and corresponding fast Fourier transformation (FFT) images of selected areas show that nanocrystals are hcp α-Nd (see Supplementary Fig. S6). In sample C2, back-scattered SEM image shows region A and region B with different contrast (see the inset in Fig. 3c). TEM results show that regions A and regions B have similar microstructure, that is, hcp α-Nd phase of 10–40 nm in size embedded in amorphous matrix (Fig. 3c and d). The grain size of hcp α-Nd phase in melt-spun $Nd_{60}Fe_{30}Al_{10}$ ribbons was smaller than that in rod sample. Increasing wheel speed decreased the grain size of hcp α-Nd phase (Table 1).

APT was employed for further investigation of the amorphous and Nd phases. In three samples, isoconcentration surfaces of 75 at.% Nd was used to visualize and identify Nd particles (Fig. 4a–d). Morphology of the Nd particles in sample M10 is granular (Fig. 4a), whereas it is flake-like

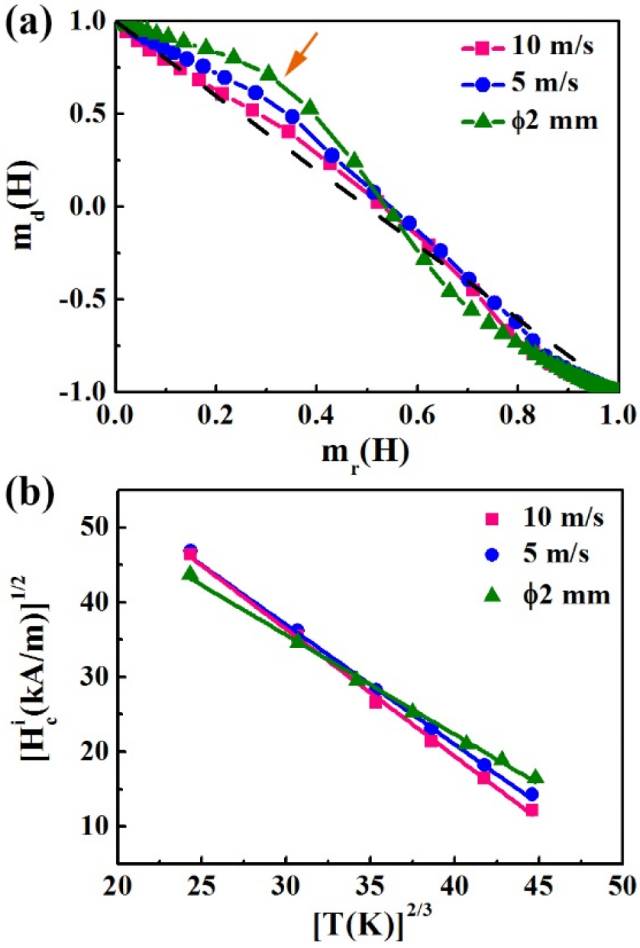

Fig. 2. Henkel plots (a) and $(H_c^i)^{1/2}$ as a function of $T^{2/3}$ in the temperature range of 120–300 K (b) for melt-spun $Nd_{60}Fe_{30}Al_{10}$ samples prepared at the wheel speed of 10 m/s (■), 5 m/s (●), and as-cast $Nd_{60}Fe_{30}Al_{10}$ rod sample of 2 mm in diameter (▲).

in sample M5 (Fig. 4b). For regions A and B in sample C2 (Fig. 4c and d), the morphology of Nd particles is flake-like, similar to that observed in sample M5. In order to identify the amorphous phase of sample M10, the concentration depth profile was obtained from the selected volume within a cylinder of a diameter of 10 nm and length of 150 nm in Fig. 4a. In the analyzed amorphous region, the concentration of Nd, Fe and Al are 57 ± 2 at.%, 32 ± 2 at.% and 11 ± 1 at.%, see Fig. 4e. It is close to the nominal composition of $Nd_{60}Fe_{30}Al_{10}$ considered as amorphous phase (indicated by two dashed lines in Fig. 4e). In other amorphous regions, the chemistry is almost identical, indicating that the composition fluctuation among the amorphous regions changes marginally in M10. For sample M5, two amorphous phases with different composition (marked as a dash line) are observed within a cylinder of 10 nm × 10 nm × 50 nm (Fig. 4f). The amount of Fe in the left region of the dash line is 48 ± 2 at.%, which is higher than that of Nd (40 ± 2 at.%), indicating that the amorphous phase is Fe-rich with an approximate composition of $Nd_{40}Fe_{48}Al_{12}$. In contrast, the right region of the dash line is Nd-rich because the composition of Fe (41 ± 2 at.%) is lower than that of Nd (48 ± 2 at.%). The composition of Nd-rich amorphous phase is about $Nd_{48}Fe_{41}Al_{11}$. That is, the composition fluctuation of amorphous phase results in the formation of Fe-rich and Nd-rich amorphous regions in sample M5. For sample C2, in region A with selected cylinder of 10 nm × 10 nm × 70 nm, the amorphous phase is Fe-rich, see Fig. 4g. The amount of Nd, Fe and Al in amorphous phase is 46 ± 2 at.%, 42 ± 2 at.% and 12 ± 1 at.%, respectively. In region B with a cylinder size of 10 nm × 10 nm × 50 nm, the amount of Nd, Fe and Al in amorphous phase is 59 ± 2 at.%, 31 ± 2 at.% and 10 ± 1 at.%, respectively, close to the nominal composition of $Nd_{60}Fe_{30}Al_{10}$ (Fig. 4h).

4. Discussion

In our work, the microstructure of ribbon and rod samples consists of amorphous phase and Nd crystal phase. Moreover, hcp Nd phase (T_C = 19 K) [20] exhibits paramagnetic behavior at room temperature, which is different from the matrix. Hence, Nd crystalline phase can act as the pinning center according to the definition of pinning centers in Gaunt's model [9]. Furthermore, when the size of particles or crystallites is comparable with the domain wall width, it is expected that it will pin domain walls. For samples M10, M5 and C2 in Table 1, the average sizes of Nd phase (10 ± 3 nm, 24 ± 8 nm and 25 ± 7 nm) are comparable to the domain wall width ($\delta_w \approx$ 28.0 nm, 27.1 nm and 13.0 nm) indicating that Nd phase can act as pinning centers to impede the movement of the domain wall. It is worth noting that the average size of Nd phase of sample M5 is 2.4 times of that in sample M10, whereas in both samples the maximum restoring force per pin, *f*, has almost the same value (1.4×10^{-11} N). In contrast, the average size of Nd phase of samples M5 and C2 has similar value, while *f* in rod sample C2 is 2.3 times larger than that in ribbon sample M5, suggesting that the average size of Nd phase has minor effect on the maximum restoring force per pin in the size range studied. Moreover, although the morphology of Nd phase in ribbon samples M10 and M5 is different, the value of *f* is similar ($\approx 1.4 \times 10^{-11}$ N). On the contrary, the value of *f* in the sample C2 is 3.4×10^{-11} N, larger than 1.5×10^{-11} N of sample M5, whereas the Nd particles in both samples are flake. This indicates that the grain morphology also has minor effect on the effectiveness of pinning.

The compositional difference between Fe-rich and Nd-rich amorphous phase played a major role on pinning of domain walls. For

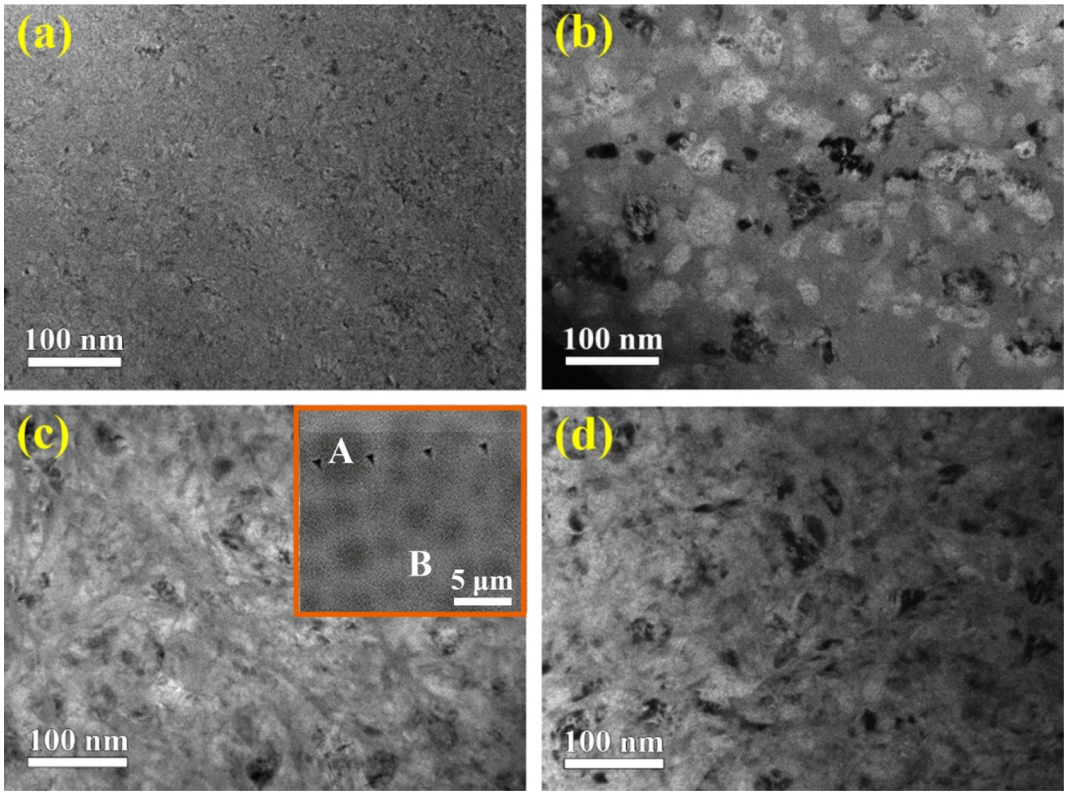

Fig. 3. The bright-field TEM images of sample M10 (a) and sample M5 (b), and region A (c) and region B (d) of sample C2.

example, in sample M10, the composition ($Nd_{57\pm2}Fe_{32\pm2}Al_{11\pm1}$) of the amorphous phase is close to the nominal composition ($Nd_{60}Fe_{30}Al_{10}$) of alloys, which indicates the composition fluctuation of amorphous phase changes marginally. For sample M5, the composition of Fe-rich amorphous phase is $Nd_{40\pm2}Fe_{48\pm2}Al_{12\pm1}$, and the composition of Nd-rich amorphous phase is $Nd_{48\pm2}Fe_{41\pm2}Al_{11\pm1}$. The content fluctuation of Nd, Fe and Al is about 8 at.%, 7 at.% and 1 at.%, respectively. For sample C2, the composition of Fe-rich amorphous phase is $Nd_{46\pm2}Fe_{42\pm2}Al_{12\pm1}$, and the composition of Nd-rich amorphous phase is $Nd_{59\pm2}Fe_{31\pm2}Al_{10\pm1}$. The content fluctuation of Nd, Fe and Al is about 13 at.%, 11 at.% and 2 at.%, respectively. The chemistry fluctuation of Nd and Fe in rod sample C2 is larger than that in ribbon sample M5. The values of maximum restoring force per pin, *f*, are 1.4×10^{-11} N, 1.5×10^{-11} N and 3.4×10^{-11} N for samples M10, M5 and C2, respectively. It indicates that the greater chemistry fluctuation leads to larger pinning force, resulting in higher coercivity in sample C2.

The origin of magnetic interaction is continuously debated in Nd-based alloys [6,21]. Our previous work of Henkel plot indicated that the interaction occurred between two amorphous phases with different composition [7,16]. The maximum restoring force per pin, *f*, has almost same value with 1.4×10^{-11} N in ribbon samples M10 and M5 (Table 1). This suggests that the role of strong pinning of domain walls is similar in ribbon samples. Hence, the H_c^i increases from 169 kA/m of sample M10 to 214 kA/m of sample M5, which attributes to stronger interaction in sample M5 than that in sample M10, as shown in Fig. 2a. That is, the fluctuation of composition between Fe-rich and Nd-rich amorphous region is believed to be the main factor of magnetic interaction in sample M5, which results in the enhancement of coercivity. Similarly, the difference of content fluctuation of Nd and Fe in sample C2 is larger than that in sample M5, which results in stronger interaction in sample C2. Hence, in comparison to ribbon samples, the enhancement of coercivity for rod $Nd_{60}Fe_{30}Al_{10}$ alloy (287 kA/m) contributes to both the improvement of magnetic interaction and strong pinning of domain walls.

It is worth mentioning that the saturate state of magnetization of $Nd_{60}Fe_{30}Al_{10}$ alloy is not observed with an applied field of 1.8 T (see Fig. 1) because of noncollinear sperimagnetic structure [22]. Turtelli et al. [11] tried the applied field of 22 T to saturate $Nd_{60}Fe_{30}Al_{10}$ alloy and failed to get saturated state of magnetization. That is, obtainable laboratory magnetic fields may not reach a high enough field to enable a reliable value of saturation magnetization of $Nd_{60}Fe_{30}Al_{10}$ alloy determined from laws of approach to magnetic saturation.

The domain wall width (δ_w) and the maximum restoring force per pin (*f*) are both important parameters in strong pinning model of domain walls. From Eqs. (1) and (2), the δ_w is given by

$$\delta_w = 4b = \frac{75k_BH_0^{3/4}}{fC^{3/2}} \tag{3}$$

However, how to determine the value of δ_w and *f* has debates for $Nd_{60}Fe_{30}Al_{10}$ BAAs. Ortega-Zempoalteca et al. [5] employed

$$f = \frac{\pi M_s^2 r^2}{9\mu_0} \tag{4}$$

to determine the value of *f*, where M_s is the saturation magnetization and *r* is the radius of the spherical defect. The *f* (6.59×10^{-11} N) was obtained by assuming that $M_s = 0.77$ T and $r = 20\times10^{-9}$ m. They used Eq. (3) to get a value of $\delta_w = 8.14$ nm for $Nd_{60}Fe_{30}Al_{10}$ bulk-cylindrical rod of 3 mm in diameter. In Eq. (4), Collocott [14] used $M_s = 0.41$ T and an estimation of $r = 40$ nm to obtain a value of $\delta_w = 6.2$ nm in $Nd_{60}Fe_{30}Al_{10}$ bulk-cylindrical rod of 2 mm in diameter. It is worth noting that the difference in the value of δ_w is mainly due to a paucity of data of M_s in high-magnetic fields for $Nd_{60}Fe_{30}Al_{10}$ alloy and artificial values of *r* (or the size of defect and precipitates). In our work, we ignored the values of M_s and *r* in Eq. (4) and calculated δ_w from experimental data obtained by measuring the intrinsic coercivity as a function of sweeping rate of applied field as described in Supplementary Fig. S3. Our estimated value of δ_w was 13 nm for sample C2. This value is higher than 8.14 nm and 6.2 nm of $Nd_{60}Fe_{30}Al_{10}$ BAAs

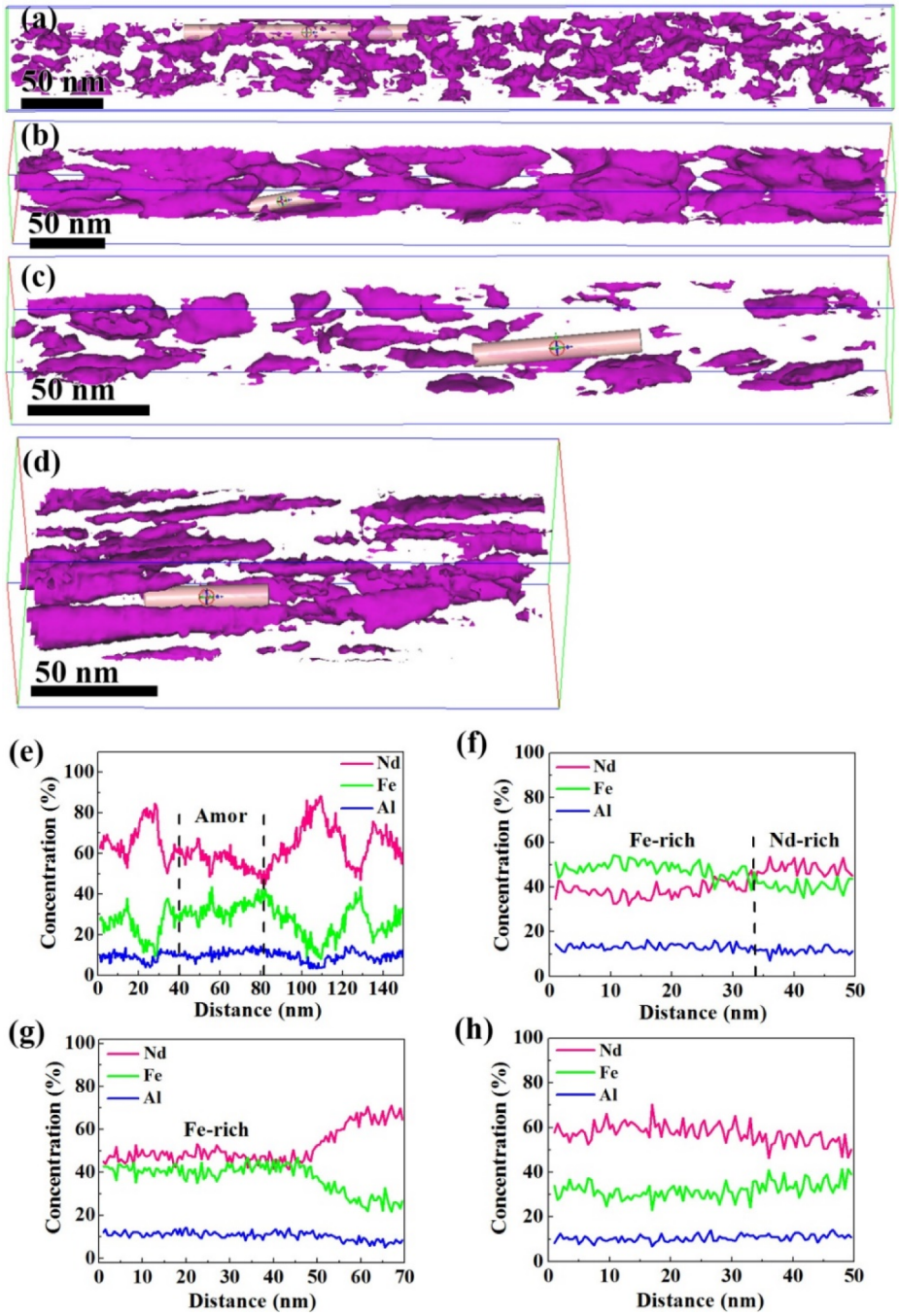

Fig. 4. Atom probe tomography (APT) results of $Nd_{60}Fe_{30}Al_{10}$ alloys. APT reconstruction illustrates segregation by isoconcentration surface of 75 at.% Nd of sample M10 (a), sample M5 (b), region A of sample C2 (c), and region B of sample C2 (d). The corresponding concentration depth profiles obtained from the selected analyzed volumes are for sample M10 (e), sample M5 (f), region A (g) and region B (h) of sample C2.

reported in Refs 5 and 14, respectively.

In addition to rod samples of 2 mm in diameter (samples C2), we also prepared rod samples of 3 mm and 5 mm in diameter. It is found that the rod sample of 3 mm in diameter has the H_c^i of 268 kA/m, close to 287 kA/m of sample C2. Moreover, the rod samples of 3 mm and 2 mm in diameter have similar microstructure with nanocrystals embedded in the amorphous phase [8]. However, we failed to obtain amorphous microstructure in rod samples of 5 mm in diameter resulting in a significant decrease of H_c^i.

The coercivity of bulk $Nd_{60}Fe_{30}Al_{10}$ alloy (C2 sample) is 287 kA/m, which is close to 290 kA/m of MnBi alloy, and higher than 46 kA/m of AlNiCo 3($Fe_{60}Ni_{27}Al_{13}$) and 180 kA/m of isotropic bonded $SrFe_{12}O_{19}$ [3]. Our previous work showed that the remanence was improved by substitution of Fe for Nd, however, the magnetic behavior changed from hard magnetic to soft magnetic with Fe content more than 50 at.% [23]. Whilst it is acknowledged that the magnitude of the remanence of $Nd_{60}Fe_{30}Al_{10}$ alloy makes it unlikely used as a hard magnet in technical applications, this type of alloy, nonetheless, is a nice model system for exploring ideas relating to the abnormal magnetic behavior and origin of coercivity in amorphous at room temperature. It can give additional remarks on related coercivity mechanism of hard magnetic materials.

5. Conclusions

Reducing the cooling rates increased the H_c^i of $Nd_{60}Fe_{30}Al_{10}$ alloys by about 70% from 169 kA/m of sample M10 to 287 kA/m of sample

C2. The coercivity of the alloys originates from the combination of magnetic interaction and strong pinning of domain walls. The pinning centers were Nd nanocrystals embedded in the amorphous matrix. The grain morphology and the size of Nd nanocrystals (< 30 nm) had minor effects on the maximum restoring force per pin. The compositional variations between Nd-rich and Fe-rich amorphous regions can be used to improve the magnetic interaction and to enhance the maximum restoring force per pin of Nd nanocrystals (with size < 30 nm embedded in amorphous matrix). Our findings give further insight into the coercivity mechanism of Nd-based amorphous ferromagnetic materials and provide a new idea to design prospective permanent alloys with good magnetic properties.

Acknowledgements

The authors thank Pengfei Hu, Jianchao Peng, Xue Liang and Bo Lu of the Instrumental Analysis & Research Center, Shanghai University, China for their assistance in TEM measurements. The authors also thank Wenqing Liu for his help about APT data analysis. This work was supported by the National Natural Science Foundation of China (grant number 51471101) and Special Fund for Instrument and Chemistry from Science and Technology Commission of Shanghai (grant number 17142203100). Part of the work was undertaken in the National High Magnetic Field Laboratory, which was supported by the US NSF (Grant NSF DMR-1644779) and by the State of Florida.

Conflicts of interest

None.

Appendix A. Supplementary data

Supplementary data to this article can be found online at https://doi.org/10.1016/j.jmmm.2019.03.059.

References

[1] A. Inoue, T. Zhang, W. Zhang, A. Takeuchi, Bulk Nd-Fe-Al amorphous alloys with hard magnetic properties, Mater. Trans. JIM 37 (1996) 99–108.
[2] A. Inoue, T. Zhang, A. Takeuchi, W. Zhang, Hard magnetic bulk amorphous Nd-Fe-Al alloys of 12 mm in diameter made by suction casting, Mater. Trans. JIM 37 (1996) 636–640.
[3] R. Skomski, J.M.D. Coey, Permanent Magnetism, Institute of Physics Publishing, Bristol and Philadelphia, 1999.
[4] S. Schneider, A. Bracchi, K. Samwer, M. Seibt, P. Thiyagarajan, Microstructure-controlled magnetic properties of the bulk glass-forming alloy $Nd_{60}Fe_{30}Al_{10}$, Appl. Phys. Lett. 80 (2002) 1749–1751.
[5] R. Ortega-Zempoalteca, I. Betancourt, R. Valenzuela, Thermomagnetic transitions and coercivity mechanism in bulk composite $Nd_{60}Fe_{30}Al_{10}$ alloys, J. Magn. Magn. Mater. 321 (2009) 3159–3163.
[6] R.W. McCallum, L.H. Lewis, M.J. Kramer, K.W. Dennis, Magnetic aspects of the ferromagnetic "bulk metallic glass" alloy system Nd-Fe-Al, J. Magn. Magn. Mater. 299 (2006) 265–280.
[7] X.H. Tan, H. Xu, H. Man, Y.J. Tang, L.P. Yang, Q. Bai, Microstructure and magnetic viscosity of bulk amorphous $Nd_{60}Fe_{20}Al_5Co_{10}B_5$ alloy, J. Appl. Phys. 109 (2011) 083927.
[8] X.H. Tan, S.J. Collocott, H.W. Liu, X.Y. Xiong, H. Xu, Structural analysis of nanocrystals and their role in the coercivity mechanism of Nd-Fe-Al-Dy bulk amorphous ferromagnets, J. Magn. Magn. Mater. 343 (2013) 27–31.
[9] P. Gaunt, Ferromagnetic domain wall pinning by a random array of inhomogeneities, Philos. Mag. B 48 (1983) 261–276.
[10] N.H. Dan, N.X. Phuc, N.M. Hong, J. Ding, D. Givord, Multi-magnetic phase behaviour of the $Nd_{60}Fe_{30}Al_{10}$ amorphous hard magnetic alloy, J. Magn. Magn. Mater. 226–230 (2001) 1385–1387.
[11] R. Sato Turtelli, D. Triyono, R. Grössinger, H. Michor, J.H. Espina, J.P. Sinnecker, H. Sassik, J. Eckert, G. Kumar, Z.G. Sun, G.J. Fan, Coercivity mechanism in $Nd_{60}Fe_{30}Al_{10}$ and $Nd_{60}Fe_{20}Co_{10}Al_{10}$ alloys, Phys. Rev. B 66 (2002) 054441.
[12] G. Kumar, J. Eckert, S. Roth, K.-H. Müller, L. Schultz, Coercivity mechanism in mold-cast $Nd_{60}Fe_xCo_{30-x}Al_{10}$ bulk amorphous alloys, J. Alloys. Compd. 348 (2003) 309–313.
[13] G. Kumar, J. Eckert, S. Roth, W. Löser, K.-H. Müller, L. Schultz, Magnetic properties of amorphous Nd-Fe-Co-Al alloys, Mater. Sci. Eng. A 375–377 (2004) 1083–1086.
[14] S.J. Collocott, Temperature dependence of the coercivity in $Nd_{60}Fe_{30-x}$ Co_xAl_{10}, x = 0 or 10, and $Pr_{58}Fe_{24}Al_{18}$ bulk amorphous ferromagnets, J. Magn. Magn. Mater. 322 (2010) 2281–2286.
[15] X.H. Tan, S.J. Collocott, H. Xu, Sweep rate and temperature dependence of the coercivity in $Nd_{60-x}Fe_{30}Al_{10}Dy_x$, x = 0, 2 and 4, bulk amorphous ferromagnets, J. Magn. Magn. Mater. 324 (2012) 2565–2571.
[16] X.H. Tan, S.F. Chan, K. Han, H. Xu, Combined effects of magnetic interaction and domain wall pinning on the coercivity in a bulk $Nd_{60}Fe_{30}Al_{10}$ ferromagnet, Sci. Rep. 4 (2014) 6805.
[17] J. García-Otero, M. Porto, J. Rivas, Henkel plots of single-domain ferromagnetic particles, J. Appl. Phys. 87 (2000) 7376–7381.
[18] E.P. Wohlfarth, Relations between different modes of acquisition of the remanent magnetization of ferromagnetic particles, J. Appl. Phys. 29 (1958) 595–596.
[19] O. Henkel, Remanenzverhalten und Wechselwirkungen in hartmagnetischen Teilchenkollektiven, Phys. Stat. Sol. 7 (1964) 919–929.
[20] R.M. Moon, J.W. Cable, W.C. Koehler, Magnetic structure of neodymium, J. Appl. Phys. 35 (1964) 1041–1042.
[21] B.C. Wei, W.H. Wang, M.X. Pan, B.S. Han, Z.R. Zhang, W.R. Hu, Domain structure of a $Nd_{60}Al_{10}Fe_{20}Co_{10}$ bulk metallic glass, Phys. Rev. B. 64 (2001) 012406.
[22] J.M.D. Coey, Amorphous magnetic order, J. Appl. Phys. 49 (1978) 1646–1652.
[23] Q. Bai, H. Xu, X.H. Tan, S.Y. Zhang, Y.D. Dong, Magnetic properties of the Fe-Nd-Al alloys prepared by suction casting, J. Mater. Sci. 42 (2007) 8248–8250.

Xiaohua Tan[a,*], Qin Deng[a], Hui Xu[a], Hui Li[a], Heyun Li[a], Zbigniew H. Stachurski[b], Ke Han[c,*]

[a] *School of Materials Science and Engineering, Shanghai University, PO BOX 269, No.149 Yanchang Road, Jingan District, Shanghai 200072, PR China*

[b] *College of Engineering and Computer Science, Australian National University, Canberra ACT 0200, Australia*

[c] *National High Magnetic Field Laboratory, Florida State University, 1800 E. Paul Dirac Drive, Tallahassee, FL 32310, USA*

E-mail addresses: tanxiaohua123@shu.edu.cn (X. Tan), han@magnet.fsu.edu (K. Han).

* Corresponding authors.